

MBE growth of $2H$ -MoTe₂ and $1T'$ -MoTe₂ on 3D substrates

Suresh Vishwanath,^{1,2, a)} Aditya Sundar,³ Xinyu Liu,⁴ Angelica Azcatl,⁵ Edward Lochocki,⁶ Arthur R. Woll,⁷ Sergei Rouvimov,² Wan Sik Hwang,² Ning Lu,⁵ Xin Peng,⁵ Huai-Hsun Lien,³ John Weisenberger,² Stephen McDonnell,^{5,8} Moon J. Kim,⁵ Margaret Dobrowolska,⁴ Jacek K Furdyna,⁴ Kyle Shen,^{6,9} Robert M. Wallace,⁵ Debdeep Jena,^{1,2,3} and Huili Grace Xing^{1,2,3,9, b)}

¹⁾*School of Electrical and Computer Engineering, Cornell University, Ithaca, NY-14853*

²⁾*Department of Electrical Engineering, University of Notre Dame, IN-46556*

³⁾*Department of Materials Science and Engineering, Cornell University, Ithaca, NY-14853*

⁴⁾*Department of Physics, University of Notre Dame, Notre Dame, IN-46556*

⁵⁾*Department of Materials Science and Engineering, University of Texas Dallas, Dallas, TX-75083*

⁶⁾*Department of Physics, Laboratory of Atomic and Solid State Physics, Cornell University, Ithaca, New York 14853*

⁷⁾*Cornell High Energy Synchrotron Source, Cornell University, Ithaca, NY-14853*

⁸⁾*Department of Materials Science and Engineering, University of Virginia, Charlottesville, VA-22904*

⁹⁾*Kavli Institute at Cornell for Nanoscale Science, Cornell University, Ithaca, New York 14853*

(Dated: 3 May 2017)

MoTe₂ is the least explored material in the Molybdenum-chalcogen family, which crystallizes in thermodynamically stable semiconducting $2H$ phase at $<500^\circ\text{C}$ and $1T'$ metallic phase at higher temperatures. Molecular beam epitaxy (MBE) provides an unique opportunity to tackle the small electronegativity difference between Mo and Te while growing layer by layer away from thermodynamic equilibrium. For a few-layer MoTe₂ grown at a moderate rate of ~ 6 mins per monolayer under varied Te:Mo flux ratio and substrate temperature, the boundary between the 2 phases in MBE grown MoTe₂ on CaF₂ is characterized using Reflection high-energy electron diffraction (RHEED), Raman spectroscopy and X-ray photoemission spectroscopy (XPS). Grazing incidence X-ray diffraction (GI-XRD) reveals a grain size of ~ 90 Å and presence of twinned grains. XRD, transmission electron microscopy, RHEED, low energy electron diffraction along with lack of electrical conductivity modulation by field effect in MBE $2H$ -MoTe₂ on GaAs (111) B show likelihood of excess Te incorporation in the films. Finally, thermal stability and air sensitivity of MBE $2H$ -MoTe₂ is investigated by temperature dependent XRD and XPS, respectively.

Keywords: Transition metal chalcogenide, MoSe₂, MoTe₂

I. INTRODUCTION

MoTe₂ is still a relatively unexplored transitional metal dichalcogenide (TMD) and holds great promise. MoTe₂ exists in trigonal prismatic ($2H$ structure) semiconducting phase at room temperature and metallic $1T'$ phase (monoclinic structure) at high temperatures

^{a)}Electronic mail: sv372@cornell.edu

^{b)}Electronic mail: grace.xing@cornell.edu

or metallic T_d phase (orthorhombic structure) when metastable $1T'$ is cooled to -33°C – -13°C ¹. $1T'$ and T_d crystal structures have the same in-plane crystal structures but vary in vertical stacking. Monolayer $2H$ -MoTe₂ is predicted to be among the smallest bandgap semiconducting TMDs². Using scanning tunneling spectroscopy (STS) measurements, the bandgap of monolayer $2H$ -MoTe₂ has been measured to be between 1.03 eV³ to 1.4 eV⁴. $2H$ -MoTe₂ has a close to broken band alignment with materials like SnSe₂⁵, making them attractive for tunnel based devices such as Esaki diodes⁶ and two-dimensional heterojunction interlayer tunneling field effect transistors (Thin-TFETs)^{7,8}. The $1T'$ structure is metastable at room temperature when the bulk MoTe₂ crystal is quenched rapidly. The T_d -MoTe₂ is a type II Weyl semimetal¹, which is a new class of topological material. Traditionally, the transition between $2H$ and $1T'$ phase was thought to be abrupt with respect to temperature⁹ but recently a mixed phase region has been observed in the phase diagram¹⁰. The transition between the $2H$ and $1T'$ phase holds promise for applications such as low resistance contacts¹¹ and phase change memory.

Large area, phase-pure epitaxial growth with layer controllability would enable industrial applications, but growth of MoTe₂ is especially challenging, since the electronegativity difference between Mo and Te is just 0.3 eV^{12–14}, resulting in a weak bond. Until recently, MoTe₂ has been obtained using tellurization of e-beam deposited molybdenum or molybdenum oxide films^{15–17} or by chemical vapor transport (CVT)^{10,18}. In case of tellurizing Mo, $1T'$ -MoTe₂ phase is initially formed at 650°C , which can be converted to $2H$ -MoTe₂ by a 3 hour anneal under Te vapor¹⁶. Tellurizing MoO₃ transforms to $2H$ -MoTe₂ more readily, but one cannot be sure in achieving 100% percent reduction of oxygen. For CVT grown MoTe₂ a mixed phase is observed in the growth temperature range of 500°C to 900°C based on the tellurium content in MoTe_x¹⁰, but under ultrahigh vacuum (UHV) in non-thermodynamic equilibrium conditions, this phase boundary is unknown. For example, the formation of a new metallic nanowire phase has been recently reported upon Te loss by annealing at 400 – 500°C in UHV¹⁹. We recently demonstrated growth of $2H$ -MoTe₂ using molecular beam epitaxy (MBE) in a superlattice with MoSe₂ as well as Bi₂Te₃²⁰, where we used a growth temperature of 380°C . Growth temperature of $\sim 340^\circ\text{C}$ ²¹ or 200°C ^{3,4} have been used in other recent MBE demonstrations of $2H$ -MoTe₂ growth.

In this study, we chose 340°C to be the lower bound of growth temperature, so as to keep the growth temperature higher than the Te cell temperature ($\sim 300^\circ\text{C}$). This avoids intentional accumulation of Te, while keeping the growth temperature significantly lower than the lower bound (500°C) of the mixed phase, as suggested by the phase diagram under 1 ATM of Te vapor¹⁰. We observe that even at a substrate growth temperature as low as 340°C , the crystalline phase of the MBE-grown MoTe₂ has a sensitive dependence on Te flux in a Te rich environment. Therefore, in Section A of this paper, we present a series of 3 samples of MoTe₂ under different growth conditions and analyze the effect of substrate temperature and tellurium flux on the MoTe₂ crystal structure and stoichiometry. Here, we show that it is indeed feasible to grow phase-pure $2H$ -MoTe₂ on a CaF₂ substrate without any requirement of a post-growth anneal. In Section B we present the growth and electrical characterization of $2H$ -MoTe₂ on GaAs (111)B. The transition to GaAs was motivated by the availability of high quality epi-ready n^+ GaAs substrates necessary for characterization using techniques such as low energy electron diffraction (LEED). Table.1 summarizes the growth conditions of all the 5 samples in this study. The Mo flux is calculated using the experimentally determined growth rates while assuming zero desorption for molybdenum adatoms, which enables calculation of the Te:Mo flux ratio tabulated in Table.1 for all samples. Growth rate on CaF₂ is calculated using cross-section transmission electron microscopy image and on GaAs (111) B from Reflection high-energy electron diffraction (RHEED) oscillations.

TABLE I. Growth conditions for all samples in this study

Series	Sample ID	Substrate	MoTe ₂ Phase	Substrate Temperature (°C)	Te Flux (Torr)	Te:Mo flux ratio	Growth duration (mins)	Post growth anneal
A	A	CaF ₂ (111)	2H	340	6.5×10^{-6}	297	30	none
	B	CaF ₂ (111)	2H+1T'	340	2.0×10^{-6}	98	30	none
	C	CaF ₂ (111)	1T'	400	1.4×10^{-6}	71	30	none
B	D	GaAs (111) B	2H	340	6.9×10^{-6}	175	30	at 380°C for 10 mins without Te
	E	GaAs (111) B	2H	340	6.9×10^{-6}	262	20	at 450°C for 3 mins and 550°C for 7 mins under Te

II. SECTION A : MoTe₂ on CaF₂

A. Growth conditions

Three samples (see Table.1) constitute the series of samples grown on CaF₂. Calcium fluoride was chosen as a substrate because (i) it has an inert fluorine-terminated surface on which we have successfully grown MoSe₂²² and (ii) it provides a cavity effect enhancing the Raman signal due to its optical transparency. On the other hand, the Raman signal from MoTe₂ grown on GaAs(111)B is very weak²⁰. These samples were grown in a Riber 32 MBE system using elemental Mo delivered from an e-beam evaporator and elemental uncracked Te from a Knudsen cell. The growth duration was 30 mins for each sample and the Mo flux, which limits the growth rate, was set to ~ 0.17 monolayer (ML) per minute or 6 minutes per ML. Supplementary (SI) Fig.1 shows that all CaF₂ substrates were first heated to 800°C, held for 30 mins in order to anneal and degas. Sharp RHEED streaks of CaF₂ prior to start of growth (see Fig.1(a)), show the smooth crystalline post-anneal growth surface. Then the substrates were lowered to respective growth temperatures, stabilized for ~ 30 mins prior to thin film growth. The growth conditions are listed in Table.1. Using these 3 samples, we observe that, although the Te flux is 2 orders of magnitude higher than the Mo flux, the Te flux range to obtain $2H$ -MoTe₂ is narrow and the substrate temperature control is critical. None of the MoTe₂ films on CaF₂ have been annealed in order to avoid phase change during annealing. All temperatures given in this study are thermocouple temperatures and the sample surface temperature is estimated about 20°C lower than the thermocouple temperature.

B. Results and discussion

1. Reflection high-energy electron diffraction (RHEED)

As seen in Fig.1(c), annealed CaF₂ has a strong streaky RHEED pattern prior to growth. Sample A shows a more diffused but still streaky RHEED pattern, whereas sample B shows a mixed pattern comprising of streaks and a ring, which evolves into only a ring in sample C. Streaky RHEED points to layered growth with minimal mosaicity of the as-grown film, but progressive inclusion of a ring points to another growth mechanism taking over, which results in polycrystalline growth. Whether the polycrystalline material is the same phase as the streaky film or a different phase is elucidated through employing Raman and XPS characterization (described below). The RHEED streaks of MoTe₂ in sample A along $\langle 11\bar{2}0 \rangle$ appear at the same position as the $\langle 1\bar{1}0 \rangle$ of CaF₂, as observed previously in MoSe₂ on CaF₂^{22,23}. The lattice spacing of MoTe₂ based upon the ratio of the RHEED streak spacing is ~ 3.5 Å, which is very close to the value of 3.52 Å¹⁰ corresponding to bulk $2H$ -MoTe₂. The ambiguity in this measurement is due to the diffused RHEED pattern, which is measured more accurately using grazing incidence X-ray diffraction (GI-XRD), presented further below.

2. Raman Spectroscopy

Raman spectra in Fig.2 confirm an evolution from the $2H$ phase to a new phase as we progress from sample A to sample C. The $2H$ phase is confirmed by comparing Raman from sample A with Raman from CVT grown bulk $2H$ -MoTe₂ obtained from 2D Semiconductors Inc. as shown in Table.2. Its important to note that the FWHM of the peaks from MBE grown MoTe₂ is several times wider than that of the CVT-grown MoTe₂. This points to a significant disorder in the MBE-grown material and augments the observation of the diffuse MoTe₂ RHEED pattern in sample A. The new phase is assigned to the $1T'$ phase due to its proximity to the peak position reported for $1T'$ in literature¹⁶. So far, only $2H$ and

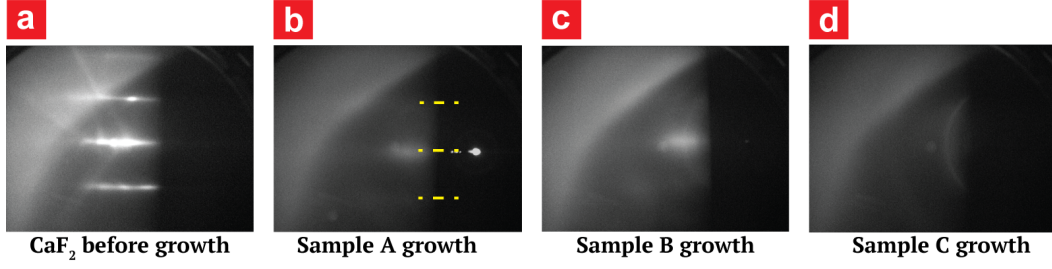


FIG. 1. (a-d) RHEED pattern from the series of samples on CaF₂ showing that $1T'$ phase grows polycrystalline as compared to well-aligned growth of $2H$ phase.

TABLE II. Positions of the various Raman peaks compared to measured values for bulk $2H$ -MoTe₂ and reported values for $1T'$ -MoTe₂¹⁶.

Sample ID	A _{1g} position (cm ⁻¹)	E _{2g} ² position (cm ⁻¹)	B _g position (cm ⁻¹)	A _g position (cm ⁻¹)
Bulk $2H$	174.47	235.80	NA	NA
A	173.30	235.79	NA	NA
B	174.14	236.66	158.07	255.59
C	NA	NA	159.14	256.23
$1T'$ ¹⁶	NA	NA	163	256.1

$1T'$ or Td phases of MoTe₂ are known. As seen in Table.2 the A_g peak position of the $1T'$ phase at 255.59 cm⁻¹-256.23 cm⁻¹ agrees closely with the reported value of 256.1 cm⁻¹ - 257 cm⁻¹ for $1T'$ MoTe₂ growth by tellurization of molybdenum films but the B_g peak at 158.07 cm⁻¹-159.14 cm⁻¹ deviates significantly from the reported value of 163 cm⁻¹ - 161 cm⁻¹ and extremely broad¹⁶¹⁵. Sample B shows a mixed phase comprised of Raman signatures from both phases, where as sample C only shows $1T'$ peaks.

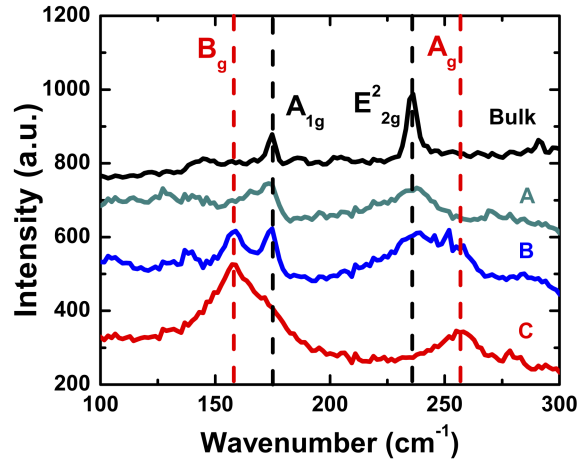


FIG. 2. (a) Raman measurements on the samples grown on CaF₂.

TABLE III. XPS peak positions for Mo $3d_{5/2}$ and Te $3d_{5/2}$ as well as Te:Mo ratio corresponding to both phases $2H$ -MoTe₂ and $1T'$ -MoTe₂ compared to reported values

Sample ID	Te:Mo flux ratio	Mo $3d_{5/2}$ $2H$ (eV)	Te $3d_{5/2}$ $2H$ (eV)	Mo $3d_{5/2}$ $1T'$ (eV)	Te $3d_{5/2}$ $1T'$ (eV)	Te:Mo _{2H} ratio w/o corr.	Te:Mo _{2H} ratio corr.	Te:Mo _{1T'} ratio w/o corr.	Te:Mo _{1T'} ratio corr.
Bulk $2H$		227.8 (air exposed ¹³) 228.0 (as cleaved ¹³) 227.8 (as cleaved ¹²)	572.9 (air exposed ¹³) 573.0 (as cleaved ¹³) 572.4 (as cleaved ¹²)						
A	297	227.9	572.8				2.03		
B	98	227.9	572.9	227.4	572.6	2.03	2.57		
C	71	228	572.9	227.5	572.6	2.04	2.54	2.12	2.66
$1T'$				227.7 ²⁴ 228 ¹⁵	572.1 ²⁴ 572.6 ¹⁵		2.61	2.13	2.72

3. X-ray photoemission spectroscopy (XPS)

XPS spectra corresponding to Mo, Te, O, Ca, F and C are detected from all samples (Fig.3). No charging effects were detected on any of them. Peak positions for Mo $3d_{5/2}$ and Te $3d_{5/2}$ as well as Te:Mo ratio corresponding to both phases $2H$ -MoTe₂ and $1T'$ -MoTe₂ are listed in Table.3. For sample A, the Mo $3d_{5/2}$ signal corresponding to $2H$ -MoTe₂ bond was detected at 227.9 eV, which is consistent with the binding energy of $2H$ -MoTe₂ in literature¹³. The Te $3d_{5/2}$ peak corresponding to the $2H$ -MoTe₂ is observed at 572.8 eV. Molybdenum oxide in the Mo⁺⁶ state was also identified. In the Te 3d spectrum, tellurium dioxide and MoTe₂ are both detected. The Te:Mo ratio is ~ 2.57 after correction due to attenuation from the oxide overlayer. For sample B, in addition to the peaks corresponding to $2H$ -MoTe₂, Mo⁺⁶ oxide and TeO₂ are detected; the Mo $3d_{5/2}$ peak at 227.6 eV and the Te $3d_{5/2}$ peak at 572.6 eV are assigned to the $1T'$ phase. The Te:Mo ratio for the $2H$ -MoTe₂ component is calculated to be 2.03. After correction due to attenuation from the oxide overlayer the Te:Mo ratio is calculated to be 2.54. The Te:Mo ratio for the $1T'$ -MoTe₂ component in sample B is 2.12 and, when corrected for the oxide overlayer is 2.66. For sample C, there is a very small signal from $2H$ -MoTe₂ with Mo $3d_{5/2}$ at 228 eV and the corresponding peak for Te $3d_{5/2}$ at 572.7 eV. But the majority of the MoTe₂ peak intensity is from a new Mo $3d_{5/2}$ peak at 227.5 eV and Te $3d_{5/2}$ at 572.5 eV, which are assigned to chemical states associated with the $1T'$ phase of MoTe₂. The Te:Mo ratio corresponding to $1T'$ phase of MoTe₂ is 2.13 and, when corrected for the oxide overlayer is 2.72. The Te:Mo ratio for the $2H$ -MoTe₂ component is 2.04 and, when corrected for the oxide overlayer, is 2.61. It is key to note that in sample C the Mo 3d peak intensity associated with Mo oxide is much higher than that for MoTe₂, as well as the oxide intensity from the other samples. This suggests that, inspite of employing a large over pressure of uncracked Te (dimers) during growth, not only does Mo form predominantly $1T'$ -MoTe₂ but that majority of Mo has an increased propensity for oxidation. This molybdenum oxide in sample C exhibits 2 different Mo oxidation states of +5 and +6. Reported peak position for $1T'$ -MoTe₂ for Mo $3d_{5/2}$ is 227.7-228 eV and for Te $3d_{5/2}$ is 572.1-572.6 eV^{15,24}. The observed XPS peak from the phase assigned to $1T'$ -MoTe₂ for Te $3d_{5/2}$ is consistent with the reported value but that for Mo $3d_{5/2}$ is much lower than what has been reported for any Mo-Te bond and even metallic Mo $3d_{5/2}$ at 227.8 eV²⁵. It is also noted that in all 3 samples, the oxide peaks from Mo and Te in the O1s spectra could not be resolved because of the close proximity in electronegativity of Mo and Te¹². The O 1s spectral feature also has contributions from C-O and O-H. Fig.3(b) shows that concentration of both molybdenum oxide and tellurium oxide concentrations are higher on the surface as seen from the increase in intensity of oxides at take-off angle of 45° as compared to 80°. (A take-off angle of 80° is much more bulk sensitive than 45°.) Also, the chemical bonding state of MoTe₂ is homogeneous through the analyzed depth, as the Mo-Te peak width remains constant when changing angle. Its worthy to note that the extent of oxidation in the telluride system is much more than previously reported MBE MoSe₂²².

4. Grazing incidence X-ray diffraction (GI-XRD) and Transmission electron microscopy (TEM)

In order to get a better estimation of the inplane lattice constant as compared to the estimation using RHEED pattern, and to understand the preference of in-plane rotational orientation, grazing incidence X-ray diffraction (GI-XRD) was done. GI-XRD from sample A shows (see Fig.4(a)) an extended line corresponding to overlapped $\{10\bar{1}0\}$ and $\{10\bar{1}1\}$ set of planes of MoTe₂ and the sharp high intensity peak is from the CaF₂ substrate. The in-plane lattice constant of $2H$ -MoTe₂ calculated from the $\{10\bar{1}0\}$ peak corresponds to 3.638 Å. The full width half maximum (FWHM) of $2H$ -MoTe₂ $\{10\bar{1}0\}$ peak is calculated to be ~ 0.079 Å⁻¹ and the direct beam FWHM is ~ 0.009 Å⁻¹. By subtracting the width of the direct beam, the genuine FWHM of the $\{10\bar{1}0\}$ peak was estimated to be ~ 0.07 Å⁻¹ which translates to a grain size of ~ 92 Å²⁶. From Fig.4(b), which is an inplane $\phi(\phi)$

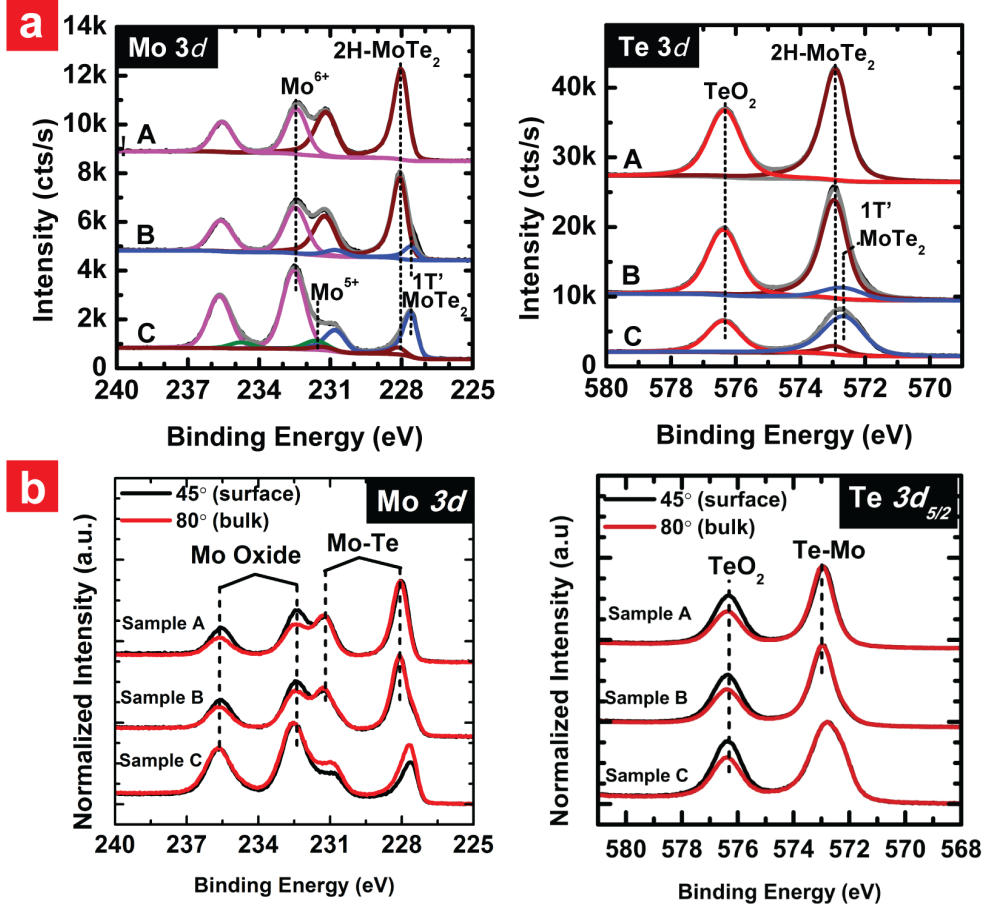


FIG. 3. (a) XPS on samples showing various phases and the extent of oxidation under various growth conditions. The pink line corresponds to Mo⁶⁺ oxide, maroon line to $2H$ -MoTe₂, blue line to $1T'$ -MoTe₂, red line to TeO₂ and green line to Mo⁵⁺ oxide (b) shows that the majority of the oxidation is limited to the surface by comparing the oxide signal from the surface and the bulk by varying the take-off angle.

scan, we can see that MBE MoTe₂ undergoes significant twinning thus showing 2 sets of 6-fold symmetry diffraction patterns. The peak ratio between adjacent peaks separated by 30° is ~ 0.5 . This shows that almost 30% of the grains are twins. Also the wide FWHM (6.7°-7.2°) of these peaks signifies a large deviation of grains from the preferred orientation. From measurements and simulation it has been shown in $2H$ -MoSe₂ that $\{10\bar{1}1\}$ and $\{10\bar{1}2\}$ peaks are ~ 10 times weaker than $\{10\bar{1}3\}$ ²⁷. $2H$ -MoTe₂ having the same crystal structure as $2H$ -MoSe₂, we also observe the $\{10\bar{1}3\}$ set of peaks at higher q_{\perp} (see Fig.4(c)), from which the out of plane lattice constant (c-spacing) is calculated to be 14.4 Å. The c axis lattice constant obtained from cs-TEM as shown in Fig.4(d) is 13.9 Å. The reported value for the inplane lattice constant and c axis lattice constant from bulk $2H$ -MoTe₂ are 3.52 Å and 13.966 Å, respectively¹⁰. To understand this discrepancy, we compare the intensity along q_{\perp} (see SI Fig.4) with simulations and observation for various polytypes of NbSe₂ by Toshihiro Shimada et al.²⁸ $2H$ -MoTe₂ and $2H$ -NbSe₂ share identical in-plane crystal structures and hence, would give similar intensity profiles along q_{\perp} for various stacking orders (polytypes). Our q_{\perp} (see SI Fig.3) scan closely matches the one reported by Toshihiro Shimada et al.²⁸ on Se-GaAs, which is explained as a combination of $2Hb$ and $3R$ NbSe₂. $2Hb$ and $3R$ both have the trigonal prismatic monolayer but the stacking sequence is different, with $3R$ having a

3-layer periodicity as compared to 2-layer for $2Hb$. The value for MBE $2H$ -MoTe₂ obtained by TEM is spatially local but X-ray beam for GI-XRD has a foot print of $\sim 2 \text{ mm} \times 10 \text{ mm}$. The excess Te measured using XPS and the presence of stacking faults resulting in mixture of $2Hb$ and $3R$ phases could be the reason for the observed larger a and c lattice constants in MBE $2H$ -MoTe₂ compared to bulk $2H$ -MoTe₂.

SI Fig.3(a) shows the cs-TEM of the mixed phase sample B. For $1T'$ -MoTe₂ is known to crystallize in $P2_1/m$ space group with lattice constants of $a=6.33 \text{ \AA}$, $b=3.48 \text{ \AA}$ and $c=13.82 \text{ \AA}$ ¹⁰, where b is very close to the lattice constant of $2H$ -MoTe₂. Therefore, for the sample C since the RHEED shows polycrystalline rings, irrespective of the in-plane rotational orientation of the film, we would expect to observe a ring corresponding to the $\{010\}$ set of planes in a similar scan as for Sample A (Fig.4(a)). SI Fig.3(c) shows the GI-XRD on sample C ie. $1T'$ -MoTe₂. SI Fig.3(c) shows that there is no signal observed corresponding to $1T'$ -MoTe₂, the only peak is corresponding to CaF₂. This is likely due to extremely low signal from the polycrystalline $1T'$ -MoTe₂ thin film. It also shows the variability in crystallinity of CaF₂ from substrate to substrate, motivating the use of epi-ready GaAs substrates in Section B.

5. Electrical measurements

Sheet resistivity of the sample A and sample C were measured to be $5468 \text{ } \Omega/\square$ and $13255 \text{ } \Omega/\square$, respectively. This is of interest because film on sample A is $2H$ -MoTe₂ and film on sample C is assigned to $1T'$ -MoTe₂. Traditionally $1T'$ -MoTe₂ should be metallic and have lower resistance than $2H$ -MoTe₂ but here the extensive oxidation of Sample C could be the cause of the significant increase in resistivity. TeO₂ glasses show semiconducting behavior²⁹.

III. SECTION B : MoTe₂ on GaAs (111)B

In this section, 2 samples (sample D and sample E) of MoTe₂ on GaAs (111)B are discussed. post-growth anneal was done on MoTe₂ films on GaAs.

A. Growth conditions for sample D

Sample D was grown at a growth temperature of 340°C and Te flux of $6.9 \times 10^{-6} \text{ Torr}$ (slightly higher than Sample A due to higher thermal conductivity of GaAs than CaF₂). SI Fig.5(a), shows the growth sequence. The key step in this growth is the anneal of GaAs under Te prior to MoTe₂ growth to achieve smoother Te terminated surface. This is consistent with our previous report of Te anneal of GaAs²⁰ prior to TMD superlattice growth. The change in growth rate between samples (see Table.1) is due to variability of Mo flux at the same e-beam power.

B. Results and Discussion

1. RHEED

For sample D, a pair of faint RHEED streaks with a spacing less than MoTe₂ were observed. Te has a hexagonal crystal structure with lattice constants of $a=4.456 \text{ \AA}$ and $c=5.921 \text{ \AA}$ ³⁰. Since the inplane lattice constant of Te is greater than that of $2H$ -MoTe₂, it was the initial suspect. With the aim to remove any excess Te in the film, a post-growth anneal at 380°C without any Te flux was done. But, as seen in SI Fig.5(b), the anneal doesn't remove this second set of streaks. Further analysis reveals that the ratio of spacing of the RHEED streaks from MoTe₂ and the newly observed streaks is ~ 2 . If the lines

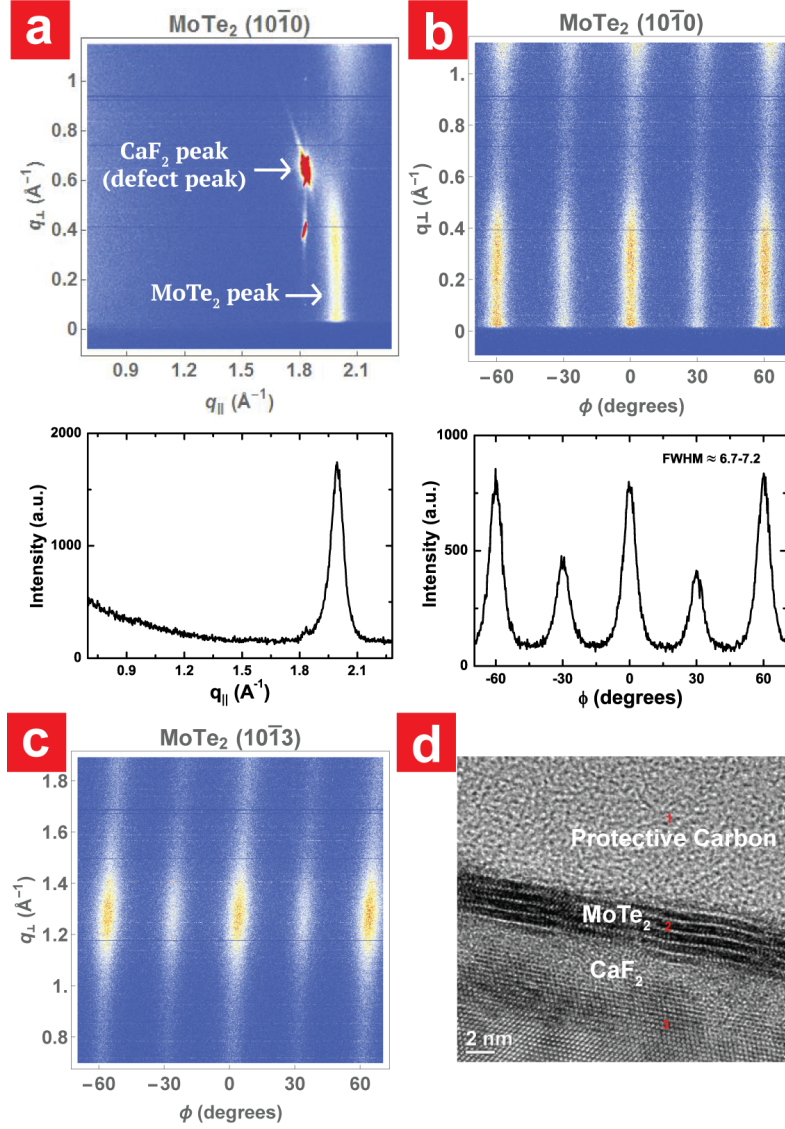


FIG. 4. For sample A (a) in-plane ω - 2θ scan showing a peak corresponding to CaF₂ and $\{10\bar{1}0\}$ of MoTe₂. The extended streak in the perpendicular direction is due to overlap of the extended rods from $\{10\bar{1}0\}$ and $\{10\bar{1}1\}$ in reciprocal space due to the ~ 5 monolayer thin film. Below it is the integrated intensity in a range of 0.02 to 0.15 Å⁻¹ q_{\perp} corresponding to $\{10\bar{1}0\}$ peak (b) The in-plane ϕ scan of the $\{10\bar{1}0\}$ peak of MoTe₂ to understand the rotational alignment and the extent of twinning in the grown film. Below it is the integrated intensity in a range of 0.02 to 0.15 Å⁻¹ q_{\perp} (c) It shows the periodicity of $\{10\bar{1}3\}$ peak. (d) cs-TEM.

were from MoTe₂ and Te, the expected ratio is ~ 1.2 . So, it's likely not due to elemental tellurium at the surface. One hypothesis is presence of ordered defects, which could be Te interstitials. Fig. 5(a) shows RHEED intensity oscillations of the RHEED spectral point during the growth of MBE $2H$ -MoTe₂. This shows close to layer by layer growth. Simulation in SI Fig. 7 shows the crest and the trough do not necessarily indicate a complete monolayer, variation in smoothness can cause shifts. But approximately, the period between crests corresponds to a monolayer. Increasing roughness or waviness in the film is the likely cause for decay with RHEED oscillation intensity in Fig. 5(a).

2. Surface morphology, XRD and TEM

It is very interesting to note that after cooling to room temperature, sample D shows Te crystallites on the surface. From AFM image (Fig.5(c)) and SEM image (SI Fig.6(a)) we can observe that these crystallites have preferential crystallographic orientation with the underlying GaAs (111) with triangular symmetry. Also, we find that the height of these crystallites is ~ 9 nm and about ~ 50 nm wide. The fact that these crystallites are purely tellurium is confirmed by the markedly distinct lattice spacing compared to MoTe₂ as seen in the high resolution transmission electron microscopy (HRTEM) image shown in Fig.5(d). This is further confirmed by TEM Energy-dispersive X-ray spectroscopy (not shown). The HRTEM image (Fig.5(d)) also shows a high quality of MoTe₂ with a c-axis lattice spacing of 13.9 Å consistent with $2H$ -MoTe₂. These crystallites could have likely been formed during the cooling process to room temperature. We don't observe Te crystallite formation on films on CaF₂ (see SI Fig.2). XRD scan in SI Fig.6(b) shows that at room temperature the (004) peak for sample D appears at 24.46° , which is lower than that for bulk $2H$ -MoTe₂ and $1T'$ -MoTe₂¹⁰. It corresponds to a c-spacing of 14.52 ± 0.05 Å. It is analyzed below along with (004) peak of sample E (see Table.4).

3. Raman and electrical characterization

Since, the Raman signal from MoTe₂ on GaAs is quite weak²⁰, the as grown film was exfoliated and transferred to SiO₂/Si substrate using a scotch tape. The transfer was performed to enhance the raman signal from the MoTe₂ due to cavity effect from SiO₂ as well as to eliminate the interference from the LO phonon raman peaks from GaAs. In Fig.5(b), the peaks below 150 cm⁻¹ can be attributed to Te³¹. E_{2g} peak from transferred MoTe₂ from sample D is almost symmetric and peak position is consistent with that from bulk MoTe₂ at 235.8 cm⁻¹. The reason for broadening in the A_{1g} peak is unclear. In order to test the electrical characteristic of the transferred MBE grown MoTe₂ film, contacts were made to the transferred flake. Using backgating, no modulation was observed (see Fig.5(e and f)).

C. Growth conditions for sample E

Sample E was grown on n⁺ GaAs for characterizations requiring conducting substrate. Prior to the post-growth anneal, the growth sequence for sample E was identical to sample D. The post-growth anneal for sample E was done at 450°C for 3 mins and 550°C for 7 mins under Tellurium flux. After this post-growth anneal, the sample was cooled under Te till growth temperature of 340°C and then capped with ~ 100 nm Se during cool-down to room temperature for surface protection during sample transfer to other characterization tools.

D. Results and Discussion

1. LEED and XRD data

From the phase diagram⁹, one might expect mixed phase formation during the post-growth anneal at 550°C under Te. LEED and XRD was done to check the phase of the film grown. Prior to LEED, the Se cap was desorbed by annealing the sample in UHV at 300°C for ~ 30 minutes. A LEED pattern measured with 40 eV electrons (Fig.6(b)) shows two sets of spots with the outer hexagonal pattern corresponding to the lattice constant of $2H$ -MoTe₂ ('a' lattice constant using LEED = 3.57 ± 0.03 Å) and the inner pattern corresponding to an effective 2×2 superstructure. This is very interesting because it is consistent with the

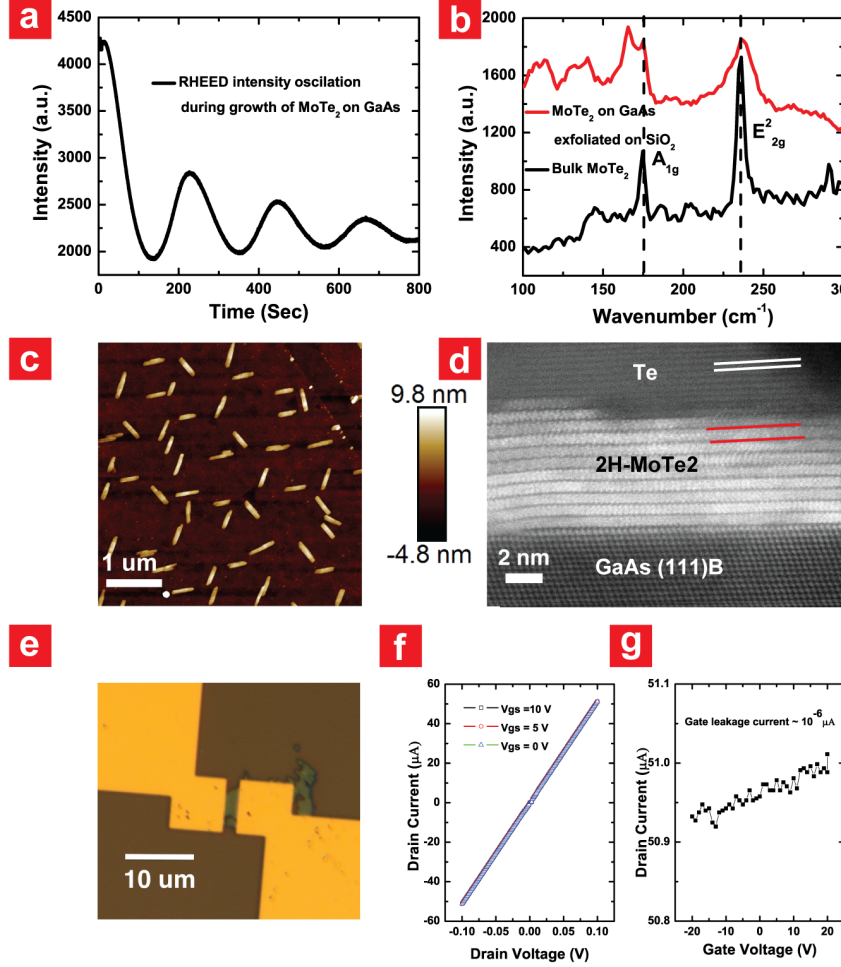


FIG. 5. Sample D: (a) RHEED oscillations at the spectral point during growth of MoTe₂ shows a close to layer by layer growth with a period of ~ 218 seconds per monolayer. (b) Raman from MoTe₂ grown on GaAs post-exfoliation, using scotch tape, on to SiO₂/Si for a better signal. (c) The surface of the thin film post-growth shows several tellurium crystallites, surprisingly with preferential direction of orientation. (d) cross-sectional TEM shows the abrupt interface between GaAs and MoTe₂, better quality of ~ 9 monolayer MoTe₂ than on CaF₂ and pure tellurium crystallite with a significantly different lattice constant and contrast. The pair of white lines and the pair of red lines are a guide to the eye marking the difference in lattice constant of Te and $2H$ -MoTe₂. (e) Optical image of the contacts fabricated to measure transistor characteristics of as grown MoTe₂. (f) shows the variation of drain current vs drain voltage at various gate biases and (g) shows that there is no gate modulation and the behavior is similar to a metal.

second set of RHEED streaks seen for sample D in SI Fig.5(b), discussed previously. One possible explanation for the extra spots is a change in the surface periodicity relative to the bulk $2H$ -MoTe₂ crystal structure due to a reconstruction or the presence of ordered defects. An alternate possibility is that the large electron spot size (~ 1 mm) may be averaging over three domains of $1T'$ -MoTe₂ rotated by 60 degrees and 120 degrees (See SI Fig.8).

To distinguish between these possibilities, temperature dependent XRD was done on sample E. At room temperature (002), (004), (006) and (008) peak 2θ positions of the as grown film are 12.17° , 25.02° , 38.02° and 51.38° respectively. The reported room temperature 2θ positions for the (002), (004), (006) and (008) peaks for $2H$ -MoTe₂ are 12.66° , 25.48° , 38.63° and 52.34° respectively. D.H Keum et al.¹⁰ report using temperature dependent XRD that the (004) 2θ peak of $2H$ -MoTe₂ is at 25.5° at room temperature and it shifts to

TABLE IV. In-plane and out of plane lattice constants for the $2H$ -MoTe₂ samples in this study obtained by various techniques

Sample ID	RHEED (Å)	XRD (Å)	GI-XRD (Å)	LEED (Å)	TEM (Å)
A	$a = 3.5 \pm 0.1$		$a = 3.64 \pm 0.03$ $c = 14.4 \pm 0.03$		$c = 13.9 \pm 0.1$
D	$a = 3.6 \pm 0.05$	$c = 14.52 \pm 0.05$			$c = 13.8 \pm 0.1$
E	$a = 3.5 \pm 0.1$	$c = 14.25 \pm 0.04$		$a = 3.57 \pm 0.03$	
Bulk $2H$		$a = 3.52085^{10}$ $c = 13.9664^{10}$			
Bulk $1T'$		$a = 6.3274^{10}$ $b = 3.4755^{10}$ $c = 13.8100^{10}$			

slightly greater than 26° at temperatures above 600°C corresponding to (004) 2θ peak of $1T'$ -MoTe₂. In our case, the (004) 2θ peak position is much lower than both peaks ($\sim 0.5^\circ$ lower than $2H$ -MoTe₂), which corresponds to a c-spacing of $14.25 \pm 0.04\text{\AA}$, and the peaks from the film is lost above 400°C . Therefore, without a chalcogen over pressure, MBE grown MoTe₂ dissociates between 400°C and 500°C . Also, sample D (see SI Fig.6(b)) which was grown without anneal at 550°C anneal has $\sim 0.5^\circ$ lower than sample E. Peak at smaller 2θ implies larger lattice constant but its origin is unclear yet. One possible explanation is the presence of excess tellurium in the crystal, which has been previously reported for bulk crystals²⁷. The MoTe₂ phase diagram⁹ shows that $2H$ -MoTe₂ is not a line compound. The $2H$ phase of MoTe₂ can be formed inspite of a 1% sub- or super- stoichiometric incorporation of tellurium. Hence, as XRD for both samples on GaAs does not show detectable peaks from the $1T'$ -MoTe₂ phase, the 2×2 superstructure observed in LEED, is likely a surface feature rather than the presence of rotated domains of $1T'$ -MoTe₂. Lattice constants obtained from the various techniques described above have been tabulated in Table.4.

2. Sensitivity to air exposure of MoTe₂

To understand the ease of oxidation of MoTe₂, on sample E, the Se cap was removed from Sample E by heating in a UHV system, followed by in situ XPS. After the initial XPS measurements, the sample was exposed to air for 20 mins and then XPS done again. It can be clearly seen from Fig.6(a) that oxide peaks appear in both Mo and Te XPS spectrum. Approximately, 8% of the surface area under goes oxidation in 20 mins. Therefore, through the process of exfoliation and fabrication the film is likely to undergo extensive oxidation. For TeO₂ glasses the conductivity goes down with lowering temperature but the conduction mechanism is by charge hopping²⁹. The Se decapping is done in an oxide MBE system that is connected to LEED and XPS system to avoid air exposure. The O 1s signal observed in XPS (see Fig.6(a)) prior to air exposure is likely due to physisorbed oxygen, post-decapping, from the oxide MBE chamber (base pressure of $\sim 1\times 10^{-8}$ Torr). This is consistent with the fact that electronegativity difference between Mo and Te is 0.3 eV but that between O and Te is 1.4 eV, making the compound prone to oxidation^{12,13}. Effect of air exposure in MBE grown films could be exacerbated by oxidation at the edges of MoTe₂ grains, similar to that reported for MBE grown WSe₂ films³².

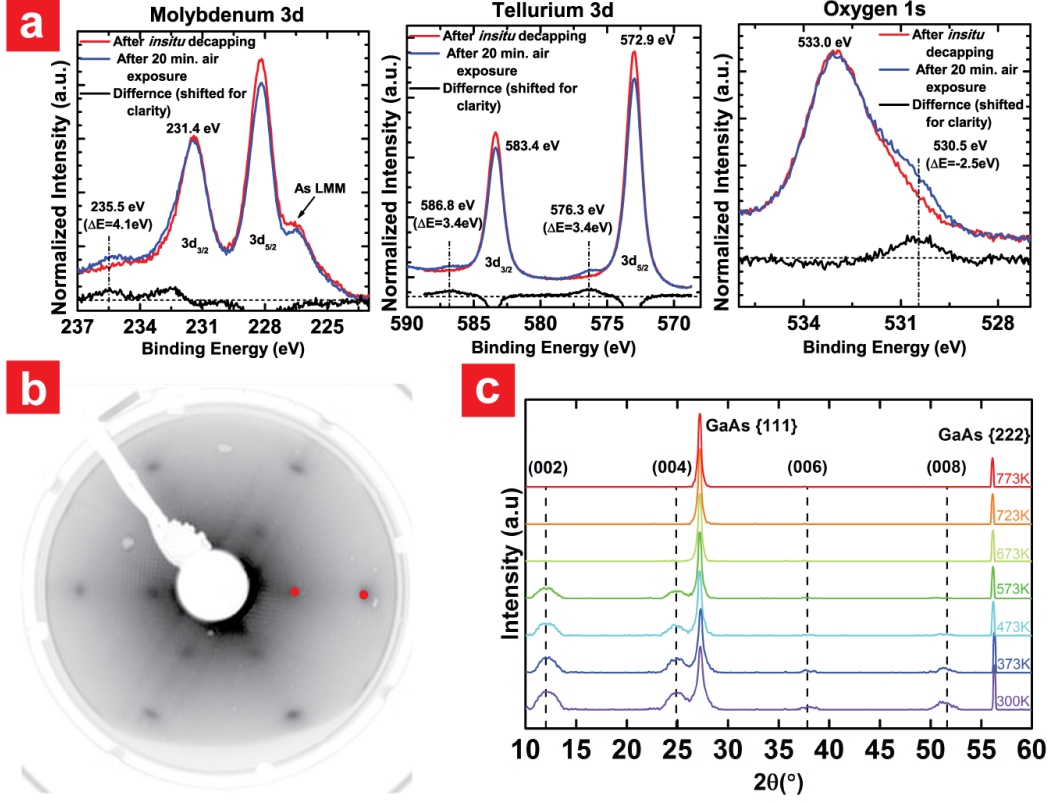


FIG. 6. (a) XPS on sample E (MoTe₂ on GaAs (111)B) post Se decapping in UHV, prior to and post-air exposure. The dash-dot lines in all 3 spectra show the emergence of the oxide peak (b) LEED from sample E post-decapping without any air exposure, the red spots are guide to the eye demonstrating the 2x2 superstructure (c) Temperature dependent XRD on sample E under nitrogen environment showing the phase of MoTe₂ and its thermal stability

IV. CONCLUSION

This work employs extensive large area structural and chemical characterization of MBE grown few layer MoTe₂, with complementing electrical characterization. In section A, we show that for growth of few layer $2H$ -MoTe₂ at a low temperature of 340°C and growth rate of ~ 6 mins/ML, we need an incident Te:Mo flux greater than 100. The $2H$ and $1T'$ phases formed in different samples have distinct signatures in RHEED, Raman and XPS, but the Te:Mo stoichiometry determined by XPS is greater than 2 for both. GI-XRD shows a small grain size of ~ 90 Å, twinning and a higher-than-expected c-spacing in $2H$ -MoTe₂ on CaF₂. XRD on MBE $2H$ -MoTe₂ on GaAs in section B also shows larger c spacing than both bulk $2H$ -MoTe₂ and bulk $1T'$ -MoTe₂. Growth on GaAs shows Te crystallite formation on the surface, and a 2x2 pattern in RHEED and LEED. All these have been hypothesized as signs of excess Te incorporation into $2H$ -MoTe₂ during growth. At ambient pressure in N₂ atmosphere, MBE $2H$ -MoTe₂ on GaAs is only stable up to 300°C. Excess Te in the film can explain the high electrical conductivity, non-modulating behaviour and easy dissociation of the film with increasing temperature prior to phase transition to the $1T'$ phase, a more stable phase at higher temperatures. Finally, we demonstrate the swift oxidation ($\sim 8\%$ surface area in 20 mins) of the MBE MoTe₂ film on exposure to air. With the various complementing large area and local characterizations, this study has provided insight into the few layer MBE growth of Mo-Te system on 3D substrates.

V. EXPERIMENTAL METHODS

1. Raman Spectroscopy

Raman measurements were performed in the backscattering configuration using a WITec Alpha 300 system at room temperature. Measurement was done using a 100x objective, 1800 grooves/mm grating, 488 nm laser and 0.75 mW power.

2. X-ray Photoelectron Spectroscopy

XPS on the CaF₂ (Series A) samples was carried out ex-situ using a monochromated Al K α source ($h\nu = 1486.7$ eV) and an Omicron Argus detector (MCD-128) operating with a pass energy of 15 eV. XPS spectra were acquired at a pass energy of 15 eV and take-off angle (defined with respect to the sample surface) of 45° and 80°. For XPS peak deconvolution, the spectral analysis software AAnalyzer was employed, where Voigt line shapes and an active Shirley background were used for peak fitting³³.

XPS on the $2H$ -MoTe₂/n⁺GaAs (Series B) samples was measured using a non-monochromated Al K α source and a Scienta R4000 electron analyzer operating at a pass energy of 100 eV. All spectra were measured at normal emission, i.e. 90 degrees relative to the sample surface. Central peak locations were determined by Lorentzian fits with linear backgrounds.

3. X-ray Diffraction

Out of plane XRD and temperature dependent XRD on the $2H$ -MoTe₂/GaAs samples is done using the Rigaku SmartLab X-Ray Diffractometer with Cu K α X-ray source. The GI-XRD is done using the G2 hutch at the CHESS beamline (<http://www.chess.cornell.edu/gline/G2.htm>), operating with a x-ray energy of 11.31 KeV.

4. Transmission Electron Microscopy

The atomic structure analysis for sample A and sample D was carried out on FEI Titan 80-300 Transmission Electron Microscope operated at 300 kV.

TEM on sample B was done using JOEL ARM200F atomic resolution analytical microscope.

5. LEED

LEED on the $2H$ -MoTe₂/n⁺GaAs samples was measured using a Specs ErLEED 3000 system with an incident electron energy of 40 eV. The electron spot size was approximately 1 mm in diameter, and the total angular field of view was 100 degrees. Following the Se decapping at 300°C, in situ LEED and XPS measurements were both performed at room temperature in an analysis chamber with pressure below $\sim 1 \times 10^{-10}$ Torr.

VI. ACKNOWLEDGMENTS

This work was supported in part by the Center for Low Energy Systems Technology (LEAST), one of six centers of STARnet, a Semiconductor Research Corporation program sponsored by MARCO and DARPA. This work made use of the Cornell Center for Materials Research Shared Facilities which are supported through the NSF MRSEC program (DMR-1120296). This work is based upon research conducted at the Cornell High Energy

Synchrotron Source (CHESS) which is supported by the National Science Foundation and the National Institutes of Health/National Institute of General Medical Sciences under NSF award DMR-1332208. MBE growth is in part supported by NSF Grant DMR 1400432 and NSF-EFRI 2DARE Grant DMR 1433490.

VII. SUPPLEMENTARY INFORMATION

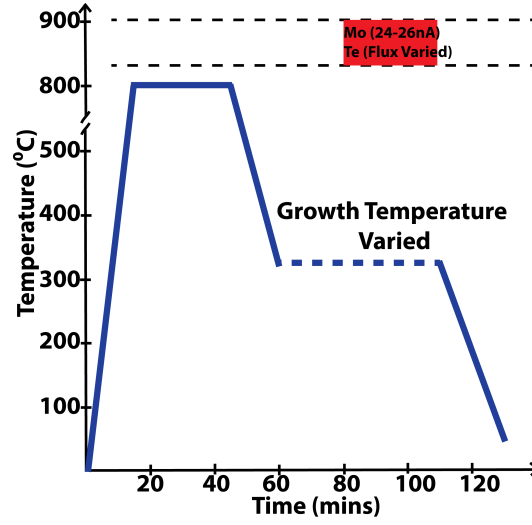


FIG. 7. General schematic of the growth diagram of MoTe₂ thin film on CaF₂.

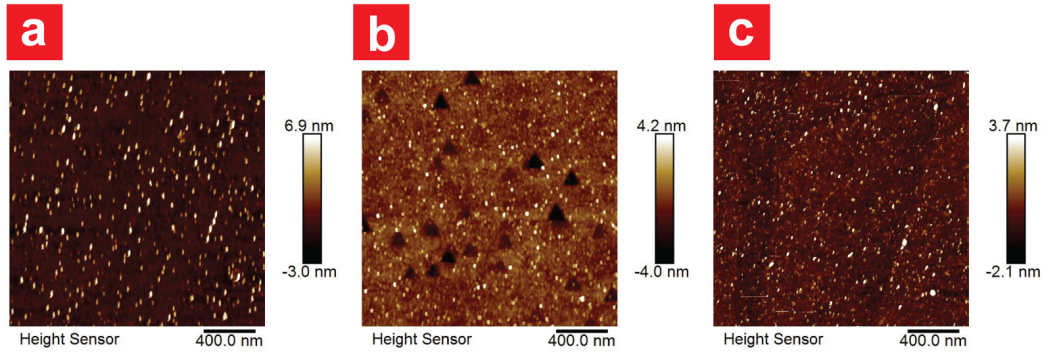


FIG. 8. AFM of (a) sample A, (b) sample B and (c) sample C.

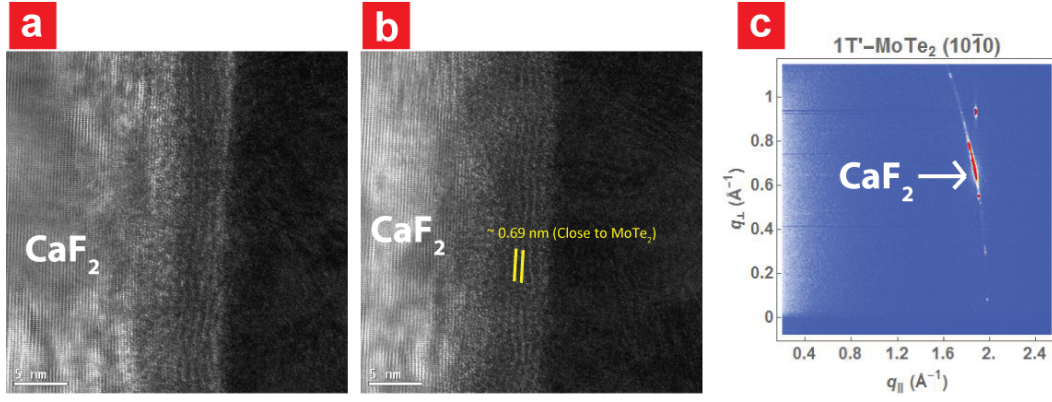


FIG. 9. (a and b)cs-HRTEM of sample B that is the mixed phase MoTe₂ and (c) GI-XRD from Sample C that is $1T'$ MoTe₂. Only signal from CaF₂ is observed, none from MoTe₂ thin film.

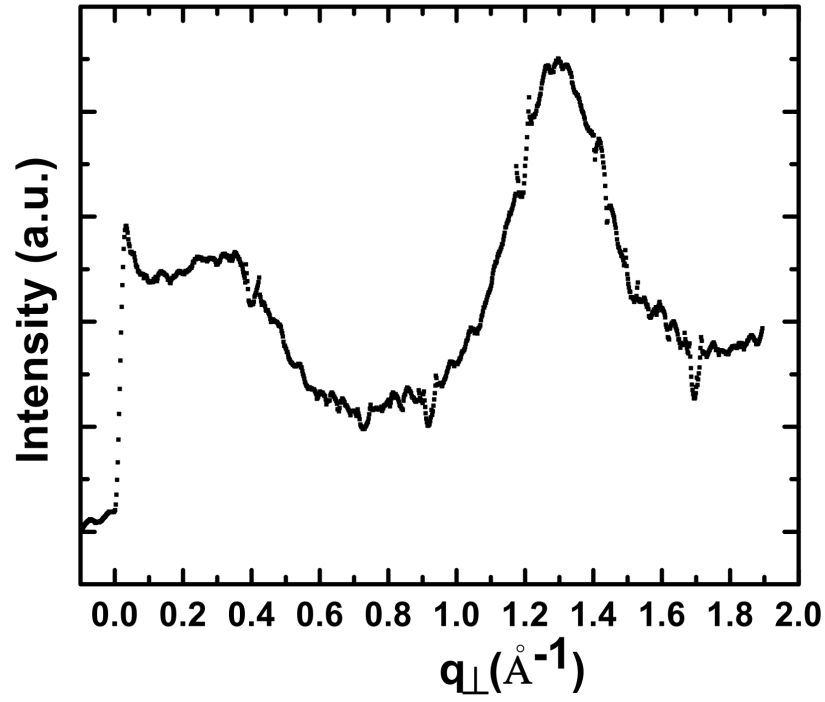


FIG. 10. Bragg rod profile for $\{10\bar{1}x\}$ peaks from $2H$ -MoTe₂ /CaF₂

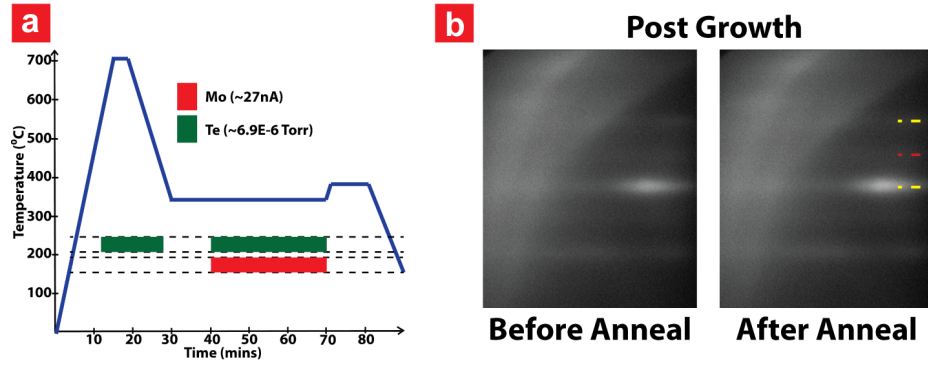


FIG. 11. (a) Growth sequence for Sample D and RHEED of MoTe₂ on GaAs post growth, (b) pre anneal and (b) post anneal. The dashed lines are guide to the eye, yellow for MoTe₂ and red for the additional set of lines observed

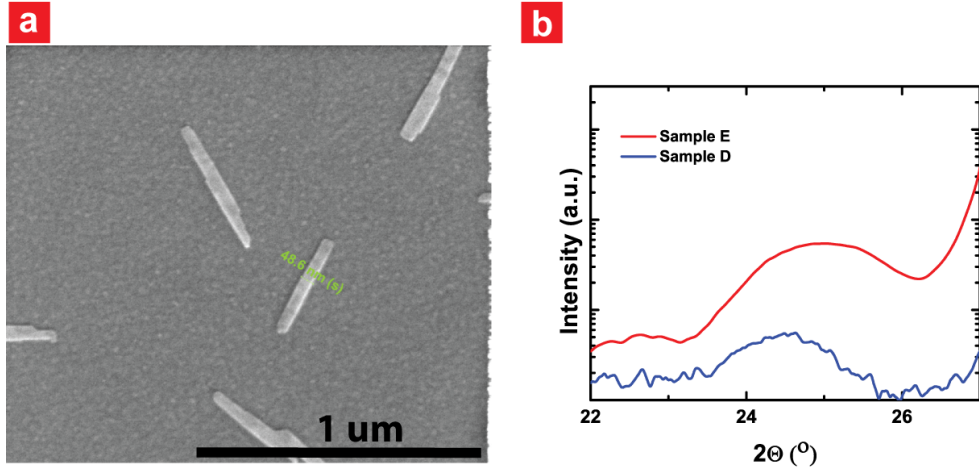


FIG. 12. (a) SEM of sample D showing electrically isolated Tellurium crystallites and (b) the zoom in of the (004) XRD peak from sample D and sample E at room temperature.

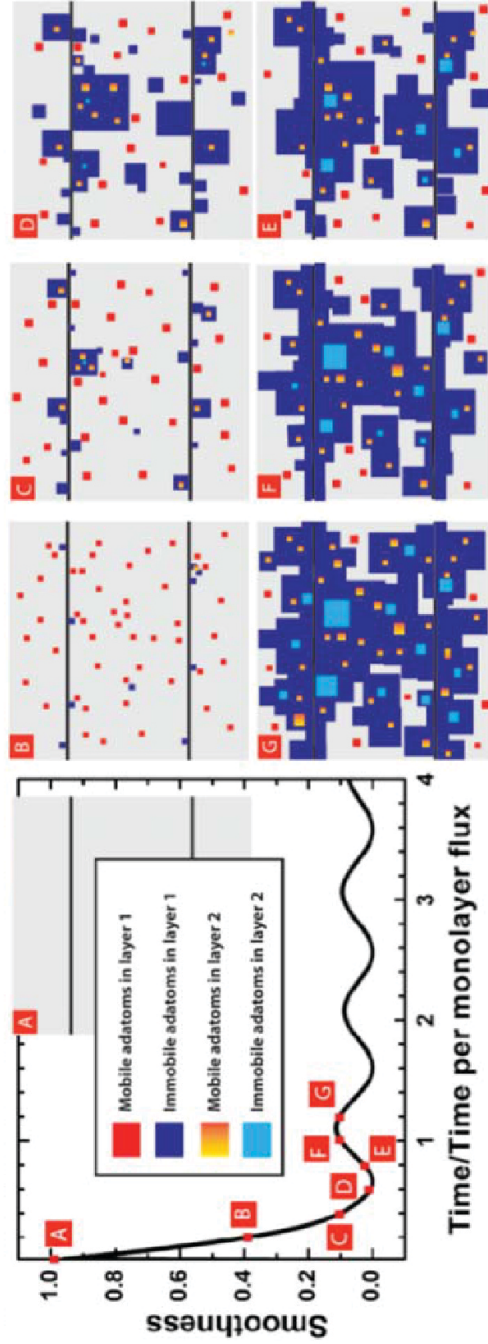


FIG. 13. Simulation of non-equilibrium surface morphology evolution following the subsection 6.3.3 of the book titled “Materials Fundamentals of Molecular Beam Epitaxy” by J.Tsao. RHEED intensity follows closely surface roughness which is a consequence of different number of layer coverage spacially. The 2 black lines corresponds to atomic steps on the substrate where nucleation could occur. In this simulation all kinetic parameters are taken to be 20/time per monolayer flux, expect for the kinetic rate constant for attachment of adatoms to the lower step edge (“down” step), which is slightly higher at 30/time per monolayer flux.

1. Possible origins of extra spots in low energy electron diffraction (LEED) patterns from bulk MoTe₂

Fig. 8a shows the crystal structure of a monolayer transition metal dichalcogenide with undistorted octahedral transition metal coordination. Lines of metal atoms run in three different directions (referred to as 1, 2, and 3; see inset of Fig. 8b), where each line is separated by a distance d . In the distorted structure, shown in Fig. 8b, the metal atoms shift, creating zigzag chains of metal atoms where two neighboring lines are separated by a smaller distance $d-\delta$. These chains run along a single direction (in this case, direction 1), causing the unit cell to change from hexagonal to rectangular symmetry. In reciprocal space, extra Bragg reflections appear corresponding to the change in symmetry (Fig. 8c and 8d). Zigzag chains along directions 1, 2, and 3 are degenerate in energy, so it is reasonable to expect domains of different orientation in a macroscopic material. In this case, if the domain size is smaller than the electron beam, a LEED experiment will measure spatially averaged patterns from all three directions (Fig. 8e). The resulting Bragg reflections are identical to those caused by a 2×2 superstructure of the original undistorted crystal. Bulk $1T'$ -MoTe₂ is formed by stacking individual monolayers with distorted octahedral Mo coordination. At a given incident electron energy, the out-of-plane periodicity determines the intensity of LEED spots but not the position of Bragg reflections. So a bulk $1T'$ -MoTe₂ sample with multiple domains would produce Bragg reflections as shown in Fig. 8e. Alternatively, a bulk $2H$ -MoTe₂ sample would produce Bragg reflections as shown in Fig. 8c. (The $2H$ structure has trigonal Mo coordination, but retains the same hexagonal symmetry assumed for Fig. 8c.) If the sample surface acquired a larger 2×2 periodicity through a surface reconstruction or the ordering of surface defects, the surface sensitivity of LEED would ensure that the resulting Bragg reflections would appear as in Fig. 8e. Because $2H$ -MoTe₂ and the distorted octahedral structures exhibit the same in-plane lattice constant, the Bragg reflections measured by LEED would appear at identical locations to bulk $1T'$ -MoTe₂ with multiple domains.

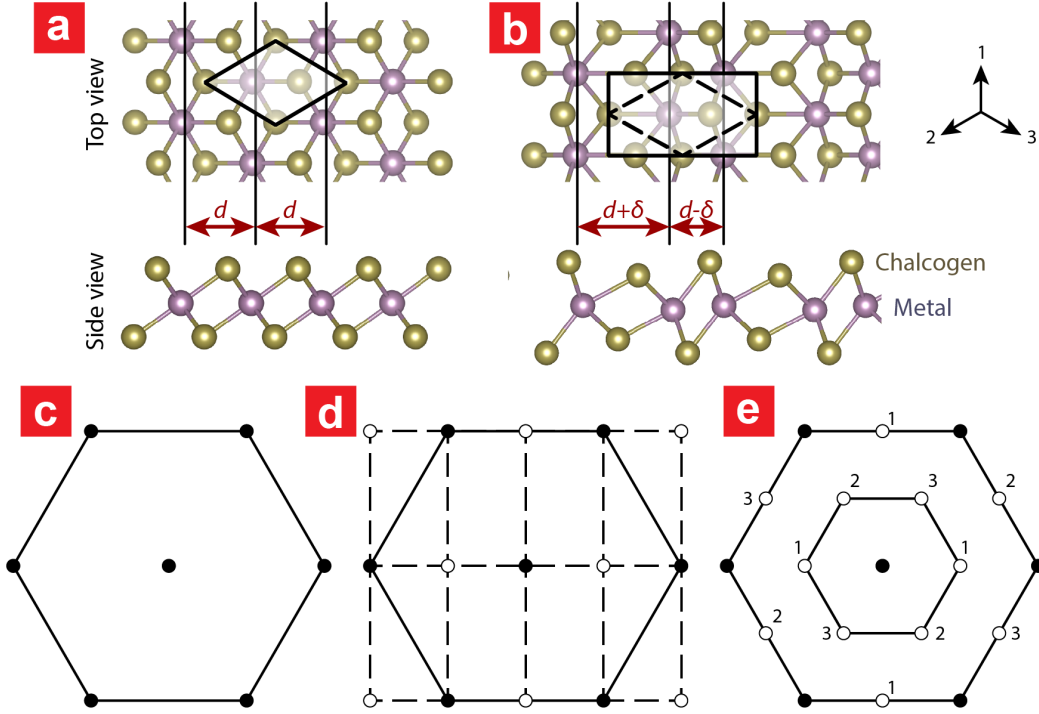


FIG. 14. (a), (b) Schematics showing crystal structures of monolayer transition metal dichalcogenides with undistorted and distorted octahedral transition metal coordination, respectively. (c), (d) Bragg reflections from the structures in (a) and (b), respectively, where filled (open) circles are from undistorted (distorted) structures. (e) Spatially averaged Bragg reflections resulting from distortions along three different directions, where the open circles are labeled according to the direction of the corresponding distortion.

VIII. REFERENCES

- ¹K. Deng, G. Wan, P. Deng, K. Zhang, S. Ding, E. Wang, M. Yan, H. Huang, H. Zhang, Z. Xu, J. Denlinger, A. Fedorov, H. Yang, W. Duan, H. Yao, Y. Wu, S. Fan, H. Zhang, C. Xi, and S. Zhou, "Experimental observation of topological fermi arcs in type-ii weyl semimetal mote2," *Nature Physics* **12**, 1105–1111 (2016).
- ²C. Gong, H. Zhang, W. Wang, L. Colombo, R. M. Wallace, and K. Cho, "Band alignment of two-dimensional transition metal dichalcogenides: Application in tunnel field effect transistors," *Applied Physics Letters* **103**, 053513 (2013).
- ³H. C. Diaz, Y. Ma, R. Chaghi, and M. Batzill, "High density of (pseudo) periodic twin-grain boundaries in molecular beam epitaxy-grown van der waals heterostructure: Mote2/mos2," *Applied Physics Letters* **108**, 191606 (2016).
- ⁴J. Chen, G. Wang, Y. Tang, J. Xu, X. Dai, J. Jia, W. Ho, and M. Xie, "Growth, stabilization and conversion of semi-metallic and semiconducting phases of mote2 monolayer by molecular-beam epitaxy," *arXiv preprint arXiv:1612.06105* (2016).
- ⁵R. Schlaf, O. Lang, C. Pettenkofer, and W. Jaegermann, "Band lineup of layered semiconductor heterointerfaces prepared by van der waals epitaxy: Charge transfer correction term for the electron affinity rule," *Journal of applied physics* **85**, 2732–2753 (1999).
- ⁶R. Yan, S. Fathipour, Y. Han, B. Song, S. Xiao, M. Li, N. Ma, V. Protasenko, D. A. Muller, D. Jena, and H. G. Xing, "Esaki diodes in van der waals heterojunctions with broken-gap energy band alignment," *Nano letters* **15**, 5791–5798 (2015).
- ⁷M. O. Li, D. Esseni, J. J. Nahas, D. Jena, and H. G. Xing, "Two-dimensional heterojunction interlayer tunneling field effect transistors (thin-tfets)," *IEEE Journal of the Electron Devices Society* **3**, 200–207 (2015).
- ⁸M. O. Li, D. Esseni, D. Jena, and H. G. Xing, "Lateral transport in two-dimensional heterojunction interlayer tunneling field effect transistor (thin-tfet)," in *Device Research Conference (DRC), 2014 72nd Annual* (IEEE, 2014) pp. 17–18.
- ⁹L. Brewer and R. Lamoreaux, "Mo-te (molybdenum-tellurium)," *Binary Alloy Phase Diagrams*, Second Edition, Ed. T.B. Massalski, ASM International, Materials Park, Ohio **3**, 2675–2676 (1990).
- ¹⁰D. H. Keum, S. Cho, J. H. Kim, D.-H. Choe, H.-J. Sung, M. Kan, H. Kang, J.-Y. Hwang, S. W. Kim, H. Yang, K. J. Chang, and Y. H. Lee, "Bandgap opening in few-layered monoclinic mote2," *Nature Physics* **11**, 482–486 (2015).
- ¹¹S. Cho, S. Kim, J. H. Kim, J. Zhao, J. Seok, D. H. Keum, J. Baik, D.-H. Choe, K. Chang, K. Suenaga, S. W. Kim, Y. H. Lee, and H. Yang, "Phase patterning for ohmic homojunction contact in mote2," *Science* **349**, 625–628 (2015).
- ¹²J. Bernede, C. Amory, L. Assmann, and M. Spiesser, "X-ray photoelectron spectroscopy study of mote 2 single crystals and thin films," *Applied surface science* **219**, 238–248 (2003).
- ¹³W. Jaegermann and D. Schmeisser, "Reactivity of layer type transition metal chalcogenides towards oxidation," *Surface science* **165**, 143–160 (1986).
- ¹⁴F. Gamble, "Ionicity, atomic radii, and structure in the layered dichalcogenides of group ivb, vb, and vib transition metals," *Journal of Solid State Chemistry* **9**, 358–367 (1974).
- ¹⁵L. Zhou, K. Xu, A. Zubair, A. D. Liao, W. Fang, F. Ouyang, Y.-H. Lee, K. Ueno, R. Saito, T. Palacios, J. Kong, and M. S. Dresselhaus, "Large-area synthesis of high-quality uniform few-layer mote2," *Journal of the American Chemical Society* **137**, 11892–11895 (2015).
- ¹⁶J. C. Park, S. J. Yun, H. Kim, J.-H. Park, S. H. Chae, S.-J. An, J.-G. Kim, S. M. Kim, K. K. Kim, and Y. H. Lee, "Phase-engineered synthesis of centimeter-scale 1t-and 2h-molybdenum ditelluride thin films," *ACS nano* **9**, 6548–6554 (2015).
- ¹⁷J. Zhou, F. Liu, J. Lin, X. Huang, J. Xia, B. Zhang, Q. Zeng, H. Wang, C. Zhu, L. Niu, X. Wang, W. Fu, P. Yu, T.-R. Chang, C.-H. Hsu, D. Wu, H.-T. Jeng, Y. Huang, H. Lin, Z. Shen, C. Yang, L. Lu, K. Suenaga, W. Zhou, S. T. Pantelides, G. Liu, and Z. Liu, "Large-area and high-quality 2d transition metal telluride," *Advanced Materials* **29**, 1603471 (1–8) (2017).
- ¹⁸J. Bernede, M. Kettaf, A. Khelil, and M. Spiesser, "p-n junctions in molybdenum ditelluride," *physica status solidi (a)* **157**, 205–209 (1996).
- ¹⁹H. Zhu, Q. Wang, C. Zhang, R. Addou, K. Cho, R. M. Wallace, and M. J. Kim, "New mo6te6 sub-nanometer-diameter nanowire phase from 2h-mote2," *Advanced Materials* (2017).
- ²⁰S. Vishwanath, X. Liu, S. Rouvimov, L. Basile, N. Lu, A. Azcatl, K. Magno, R. M. Wallace, M. Kim, J.-C. Idrobo, J. K. Furdyna, D. Jena, and H. G. Xing, "Controllable growth of layered selenide and telluride heterostructures and superlattices using molecular beam epitaxy," *Journal of Materials Research* **31**, 900–910 (2016).
- ²¹A. Roy, H. C. Movva, B. Satpati, K. Kim, R. Dey, A. Rai, T. Pramanik, S. Guchhait, E. Tutuc, and S. K. Banerjee, "Structural and electrical properties of mote2 and mose2 grown by molecular beam epitaxy," *ACS applied materials & interfaces* **8**, 7396–7402 (2016).
- ²²S. Vishwanath, X. Liu, S. Rouvimov, P. C. Mende, A. Azcatl, S. McDonnell, R. M. Wallace, R. M. Feenstra, J. K. Furdyna, D. Jena, , and H. G. Xing, "Comprehensive structural and optical characterization of mbe grown mose2 on graphite, caf2 and graphene," *2D Materials* **2**, 024007 (2015).

- ²³A. Koma, K. Saiki, and Y. Sato, "Heteroepitaxy of a two-dimensional material on a three-dimensional material," *Applied surface science* **41**, 451–456 (1990).
- ²⁴C. H. Naylor, W. M. Parkin, J. Ping, Z. Gao, Y. R. Zhou, Y. Kim, F. Streller, R. W. Carpick, A. M. Rappe, M. Drndic, J. M. Kikkawa, and A. T. C. Johnson, "Monolayer single-crystal $1t$ -mote₂ grown by chemical vapor deposition exhibits weak antilocalization effect," *Nano letters* **16**, 4297–4304 (2016).
- ²⁵F. Werfel and E. Minni, "Photoemission study of the electronic structure of mo and mo oxides," *Journal of Physics C: Solid State Physics* **16**, 6091 (1983).
- ²⁶T. Shimada, H. Nishikawa, A. Koma, Y. Furukawa, E. Arakawa, K. Takeshita, and T.-i. Matsushita, "Polytypes and crystallinity of ultrathin epitaxial films of layered materials studied with grazing incidence x-ray diffraction," *Surface science* **369**, 379–384 (1996).
- ²⁷P. James and M. Lavik, "The crystal structure of mose₂," *Acta Crystallographica* **16**, 1183–1183 (1963).
- ²⁸T. Shimada, Y. Furukawa, E. Arakawa, K. Takeshita, T. Matsushita, H. Yamamoto, and A. Koma, "Structure determination of ultrathin nbse₂ films by grazing incidence x-ray diffraction," *Solid state communications* **89**, 583–586 (1994).
- ²⁹R. Hampton, W. Hong, G. Saunders, and R. El-Mallawany, "The electrical conductivity of pure and binary teo₂ glasses," *Journal of non-crystalline solids* **94**, 307–314 (1987).
- ³⁰C. Adenis, V. Langer, and O. Lindqvist, "Reinvestigation of the structure of tellurium," *Acta Crystallographica Section C: Crystal Structure Communications* **45**, 941–942 (1989).
- ³¹A. Pine and G. Dresselhaus, "Raman spectra and lattice dynamics of tellurium," *Physical Review B* **4**, 356 (1971).
- ³²J. H. Park, S. Vishwanath, X. Liu, H. Zhou, S. M. Eichfeld, S. K. Fullerton-Shirey, J. A. Robinson, R. M. Feenstra, J. Furdyna, D. Jena, and H. G. Xing, "Scanning tunneling microscopy and spectroscopy of air exposure effects on molecular beam epitaxy grown wse₂ monolayers and bilayers," *ACS nano* **10**, 4258–4267 (2016).
- ³³A. Herrera-Gomez, A. Hegedus, and P. Meissner, "Chemical depth profile of ultrathin nitrided sio₂ films," *Applied physics letters* **81**, 1014–1016 (2002).